





















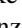



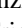
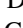
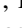
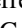


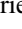






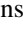

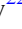
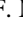


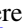
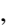







DeepZipper. II. Searching for Lensed Supernovae in Dark Energy Survey Data with Deep Learning

R. Morgan^{1,2,3} , B. Nord^{2,4} , K. Bechtol^{1,5} , A. Möller⁶ , W. G. Hartley⁷, S. Birrer^{8,9} , S. J. González¹ , M. Martínez¹ ,
 R. A. Gruendl^{10,11} , E. J. Buckley-Geer^{2,12} , A. J. Shajib^{12,56} , A. Carnero Rosell^{13,14,15} , C. Lidman^{16,17} , T. Collett¹⁸ ,
 T. M. C. Abbott¹⁹, M. Aguena¹⁴ , F. Andrade-Oliveira²⁰, J. Annis² , D. Bacon¹⁸ , S. Bocquet²¹ , D. Brooks²² ,
 D. L. Burke^{9,23}, M. Carrasco Kind^{10,11} , J. Carretero²⁴ , F. J. Castander^{25,26} , C. Conselice^{27,28} , L. N. da Costa^{14,29},
 M. Costanzi^{30,31,32} , J. De Vicente³³ , S. Desai³⁴ , P. Doel²², S. Everett³⁵, I. Ferrero³⁶, B. Flaugher² , D. Friedel¹⁰,
 J. Frieman^{2,4} , J. García-Bellido³⁷ , E. Gaztanaga^{25,26} , D. Gruen²¹ , G. Gutierrez² , S. R. Hinton³⁸ ,
 D. L. Hollowood³⁵ , K. Honscheid^{39,40} , K. Kuehn^{41,42} , N. Kuropatkin² , O. Lahav²² , M. Lima^{14,43}, F. Menanteau^{10,11} ,
 R. Miquel^{24,44} , A. Palmese⁴⁵ , F. Paz-Chinchón^{10,46} , M. E. S. Pereira⁴⁷, A. Pieres^{14,29} , A. A. Plazas Malagón⁴⁸ ,
 J. Prat^{4,12}, M. Rodríguez-Monroy⁴⁹, A. K. Romer⁵⁰ , A. Roodman^{9,23} , E. Sanchez³³ , V. Scarpine², I. Sevilla-Noarbe³³ ,
 M. Smith⁵¹ , E. Suchyta⁵² , M. E. C. Swanson⁵¹, G. Tarle²⁰ , D. Thomas¹⁸, and T. N. Varga^{53,54,55}

¹ Physics Department, University of Wisconsin-Madison, Madison, WI 53706, USA; robert.morgan@wisc.edu

² Fermi National Accelerator Laboratory, P.O. Box 500, Batavia, IL 60510, USA

³ Legacy Survey of Space and Time Corporation Data Science Fellowship Program, USA

⁴ Kavli Institute for Cosmological Physics, University of Chicago, Chicago, IL 60637, USA

⁵ Legacy Survey of Space and Time, 933 North Cherry Avenue, Tucson, AZ 85721, USA

⁶ Centre for Astrophysics & Supercomputing, Swinburne University of Technology, Victoria 3122, Australia

⁷ Department of Astronomy, University of Geneva, ch. d'Ecogia 16, CH-1290 Versoix, Switzerland

⁸ Kavli Institute for Particle Astrophysics and Cosmology, Department of Physics, Stanford University, Stanford, CA 94305, USA

⁹ SLAC National Accelerator Laboratory, Menlo Park, CA 94025, USA

¹⁰ Center for Astrophysical Surveys, National Center for Supercomputing Applications, 1205 West Clark St., Urbana, IL 61801, USA

¹¹ Department of Astronomy, University of Illinois at Urbana-Champaign, 1002 W. Green Street, Urbana, IL 61801, USA

¹² Department of Astronomy and Astrophysics, University of Chicago, Chicago, IL 60637, USA

¹³ Instituto de Astrofísica de Canarias, E-38205 La Laguna, Tenerife, Spain

¹⁴ Laboratório Interinstitucional de e-Astronomia - LIneA, Rua Gal. José Cristino 77, Rio de Janeiro, RJ—20921-400, Brazil

¹⁵ Universidad de La Laguna, Dpto. Astrofísica, E-38206 La Laguna, Tenerife, Spain

¹⁶ Centre for Gravitational Astrophysics, College of Science, The Australian National University, ACT 2601, Australia

¹⁷ The Research School of Astronomy and Astrophysics, The Australian National University, ACT 2601, Australia

¹⁸ Institute of Cosmology and Gravitation, University of Portsmouth, Portsmouth PO1 3FX, UK

¹⁹ Cerro Tololo Inter-American Observatory, NSF's National Optical-Infrared Astronomy Research Laboratory, Casilla 603, La Serena, Chile

²⁰ Department of Physics, University of Michigan, Ann Arbor, MI 48109, USA

²¹ University Observatory, Faculty of Physics, Ludwig-Maximilians-Universität, Scheinerstr. 1, D-81679 Munich, Germany

²² Department of Physics & Astronomy, University College London, Gower Street, London WC1E 6BT, UK

²³ Kavli Institute for Particle Astrophysics & Cosmology, P.O. Box 2450, Stanford University, Stanford, CA 94305, USA

²⁴ Institut de Física d'Altes Energies (IFAE), The Barcelona Institute of Science and Technology, Campus UAB, E-08193 Bellaterra (Barcelona), Spain

²⁵ Institut d'Estudis Espacials de Catalunya (IEEC), E-08034 Barcelona, Spain

²⁶ Institute of Space Sciences (ICE, CSIC), Campus UAB, Carrer de Can Magrans, s/n, E-08193 Barcelona, Spain

²⁷ Jodrell Bank Center for Astrophysics, School of Physics and Astronomy, University of Manchester, Oxford Road, Manchester M13 9PL, UK

²⁸ University of Nottingham, School of Physics and Astronomy, Nottingham NG7 2RD, UK

²⁹ Observatório Nacional, Rua Gal. José Cristino 77, Rio de Janeiro, RJ—20921-400, Brazil

³⁰ Astronomy Unit, Department of Physics, University of Trieste, via Tiepolo 11, I-34131 Trieste, Italy

³¹ INAF-Osservatorio Astronomico di Trieste, via G.B. Tiepolo 11, I-34143 Trieste, Italy

³² Institute for Fundamental Physics of the Universe, Via Beirut 2, I-34014 Trieste, Italy

³³ Centro de Investigaciones Energéticas, Medioambientales y Tecnológicas (CIEMAT), Madrid, Spain

³⁴ Department of Physics, IIT Hyderabad, Kandi, Telangana 502285, India

³⁵ Santa Cruz Institute for Particle Physics, Santa Cruz, CA 95064, USA

³⁶ Institute of Theoretical Astrophysics, University of Oslo. P.O. Box 1029 Blindern, NO-0315 Oslo, Norway

³⁷ Instituto de Física Teórica UAM/CSIC, Universidad Autónoma de Madrid, E-28049 Madrid, Spain

³⁸ School of Mathematics and Physics, University of Queensland, Brisbane, QLD 4072, Australia

³⁹ Center for Cosmology and Astro-Particle Physics, The Ohio State University, Columbus, OH 43210, USA

⁴⁰ Department of Physics, The Ohio State University, Columbus, OH 43210, USA

⁴¹ Australian Astronomical Optics, Macquarie University, North Ryde, NSW 2113, Australia

⁴² Lowell Observatory, 1400 Mars Hill Rd, Flagstaff, AZ 86001, USA

⁴³ Departamento de Física Matemática, Instituto de Física, Universidade de São Paulo, CP 66318, São Paulo, SP, 05314-970, Brazil

⁴⁴ Institució Catalana de Recerca i Estudis Avançats, E-08010 Barcelona, Spain

⁴⁵ Department of Astronomy, University of California, Berkeley, 501 Campbell Hall, Berkeley, CA 94720, USA

⁴⁶ Institute of Astronomy, University of Cambridge, Madingley Road, Cambridge CB3 0HA, UK

⁴⁷ Hamburger Sternwarte, Universität Hamburg, Gojenbergsweg 112, D-21029 Hamburg, Germany

⁴⁸ Department of Astrophysical Sciences, Princeton University, Peyton Hall, Princeton, NJ 08544, USA

⁴⁹ Centro de Investigaciones Energéticas, Medioambientales y Tecnológicas (CIEMAT), Madrid, Spain

⁵⁰ Department of Physics and Astronomy, Pevensey Building, University of Sussex, Brighton BN1 9QH, UK

⁵¹ School of Physics and Astronomy, University of Southampton, Southampton, SO17 1BJ, UK

⁵² Computer Science and Mathematics Division, Oak Ridge National Laboratory, Oak Ridge, TN 37831, USA

⁵³ Excellence Cluster Origins, Boltzmannstr. 2, D-85748 Garching, Germany

⁵⁴ Max Planck Institute for Extraterrestrial Physics, Giessenbachstrasse, D-85748 Garching, Germany⁵⁵ Universitäts-Sternwarte, Fakultät für Physik, Ludwig-Maximilians Universität München, Scheinerstr. 1, D-81679 München, Germany
Received 2022 April 11; revised 2022 May 17; accepted 2022 May 20; published 2023 January 23

Abstract

Gravitationally lensed supernovae (LSNe) are important probes of cosmic expansion, but they remain rare and difficult to find. Current cosmic surveys likely contain 5–10 LSNe in total while next-generation experiments are expected to contain several hundred to a few thousand of these systems. We search for these systems in observed Dark Energy Survey (DES) five year SN fields—10 3 sq. deg. regions of sky imaged in the *griz* bands approximately every six nights over five years. To perform the search, we utilize the DeepZipper approach: a multi-branch deep learning architecture trained on image-level simulations of LSNe that simultaneously learns spatial and temporal relationships from time series of images. We find that our method obtains an LSN recall of 61.13% and a false-positive rate of 0.02% on the DES SN field data. DeepZipper selected 2245 candidates from a magnitude-limited ($m_i < 22.5$) catalog of 3,459,186 systems. We employ human visual inspection to review systems selected by the network and find three candidate LSNe in the DES SN fields.

Unified Astronomy Thesaurus concepts: [Strong gravitational lensing \(1643\)](#); [Supernovae \(1668\)](#)

1. Introduction

Galaxy-scale gravitational lensing occurs when the gravitational potential of a foreground galaxy (positioned along an observer’s line of sight to a background galaxy) is large enough to deflect the photons of the background galaxy on their journey to an observer. This process produces arcs and/or multiple images of the background galaxy (Treu 2010). For the specific case in which the background galaxy contains a supernova (SN), the photons that contribute to each of the multiple images of the lensed supernova (LSN) travel different paths and distances to the observer and encounter different depths of gravitational potential depending on the distribution of the foreground galaxy’s mass. Because the speed of light is constant, the distinct paths correspond to distinct arrival times of the photons from each SN image. Combining this time delay with a model of the foreground galaxy’s mass distribution enables the direct inference of the rate of expansion of the universe today, H_0 , as well as other cosmological parameters (Refsdal 1964).

Historically, LSNe are rare—only a few detections have been made in total (Amanullah et al. 2011; Quimby et al. 2014; Kelly et al. 2015; Rodney et al. 2015, 2021; Goobar et al. 2017). However, modern optical time-domain survey data sets, such as those collected in the southern hemisphere by the Dark Energy Survey’s (DES; Abbott et al. 2016; Diehl 2020) SN fields, in the northern hemisphere by the Zwicky Transient Facility (Graham et al. 2019) and the Young Supernova Experiment (Jones et al. 2021), and over the next decade by the Vera C. Rubin Observatory’s Legacy Survey of Space and Time (LSST; Ivezić et al. 2019), are promising places to search for LSNe. Based on imaging depth, sky area, and duration of observations, the DES SN fields are expected to contain ~ 0.5 –2 LSNe, and the LSST wide field is expected to contain ~ 2000 LSNe (Oguri 2019). These data sets, which contain hundreds of millions to tens of billions of objects that are not LSNe, pose a significant challenge for searches (Marshall et al. 2017; Abbott et al. 2021). In particular, it is vital to identify an LSN rapidly to enable follow-up observations before the SN fades during the weeks to months after

the explosion (Mihalas 1963). To keep pace with the data streams of large surveys and identify candidate LSNe promptly, we require fast and robust algorithms.

In Morgan et al. (2022)—hereafter referred to as “DZ1”—we designed a deep learning detection architecture (“ZipperNet”) for LSNe and demonstrated its performance on four simulated optical survey data sets that mimic DES and LSST. In this work, we use a ZipperNet to search the DES SN fields (Abbott et al. 2021) for LSNe. We also discuss the data collection and data reduction steps necessary to carry out a comprehensive LSN search in an optical survey data set. We have made all code for data processing and deep learning available at DZ1.

We present this work as follows. In Section 2, we describe the characteristics of the DES SN field data. In Section 3, we describe the training and optimization of our deep learning approach. In Section 4, we quantify the performance of this architecture on the DES SN field data, as well as current candidate LSN systems. In Section 5, we discuss the significance of the results and the outlook for detecting LSNe in Rubin Observatory data. We conclude in Section 6.

2. Data Collection

2.1. The DES SN Fields

DES SN field data were collected (a) to facilitate the Type Ia SN (SN Ia) cosmology analyses in DES that use the single-epoch images and (b) to enable galaxy population modeling (near the detection limits of the DES wide-field survey) that uses coadded images. All data were collected with DECam (Flaugher et al. 2015) on the Victor M. Blanco telescope from the Cerro-Tololo Inter-American Observatory in Chile between 2012 and 2018. There are 10 3 sq. deg. fields: eight *shallow* fields (X1, X2, E1, E2, C1, C2, S1, and S2) observed to a single-visit depth of ~ 23.5 mag, and two *deep* fields (X3 and C3) observed to a single-visit depth of ~ 24.5 mag. Each field was imaged in the *griz* bands approximately every six nights over five years, subject to Sun, Moon, and weather conditions. The median full-width-at-half-maximum point-spread functions (PSFs) (“seeing”) for the SN field images used in this analysis (after the downsampling discussed in Section 2.2) were $1''.37$, $1''.26$, $1''.15$, and $1''.08$ for the *griz*.

2.2. Candidate System Selection and Data Reduction

We begin our search for candidate LSNe with all cataloged objects of DES Data Release 1 (also referred to as the “Year 3

⁵⁶ NHFP Einstein Fellow.

Original content from this work may be used under the terms of the [Creative Commons Attribution 4.0 licence](#). Any further distribution of this work must maintain attribution to the author(s) and the title of the work, journal citation and DOI.

Gold Catalog”; Abbott et al. 2018). We construct an initial sample by requiring the object to be positioned within one of the SN fields and requiring all *griz* MAG_AUTO measurements to be brighter than 27.5 mag. Then, within that sample, we require the *i* band MAG_AUTO only to be brighter than 22.5 mag to restrict the total number of objects in this first search of the DES SN fields. Also within the initial sample, we require a catalog-level parameter size measurement (CM_T) to be greater than 0.05, which excludes non-extended objects (e.g., stars) with approximately 99% galaxy purity and 98% galaxy completeness. To evaluate the purity and completeness, we take a nearest-neighbor machine-learning classifier that combines DES photometry with near-infrared photometry as truth, which has shown near-perfect performance at $mag_i < 22.5$ (Hartley et al. 2021). These cuts produce a sample of 3,459,186 candidate systems for our analysis.

We next introduce a selection on the images that are used in the LSNe search across all five years of DES SN field exposures (Abbott et al. 2021). If a system has two images on the same night in the same band, we choose the image for which the object was observed with the better seeing. For each image, we also require the cataloged object’s centroid to be positioned more than 23 pixels from all CCD edges: this permits constructing image cutouts (45 pixel by 45 pixel) without producing partial images. Finally, to enforce cadence uniformity and simplify data processing, we require the same number of observations in each of the *griz* bands. We determine the band with the fewest useful observations and exclude images from the other bands to match it. In doing so, we exclude images from regions of the time series in descending order of the sampling rate. Thus, for each candidate lens galaxy in the SN fields selected from the DES catalog, we obtain a time series image set with the same number of images in each band of *griz*. A typical length for a time series image set is ~ 20 –35 epochs. We process each year of DES data independently.

3. Deep Learning Methods

3.1. Training Set Construction

Our approach for detecting LSNe in the DES deep fields requires samples of LSNe (positives) and non-LSNe (negatives) to train the ZipperNet in a binary classification scheme. To construct the training set, we used $\sim 2\%$ of the total data set—76,203 time series image sets. Due to the lack of real LSN examples, we create the positive class using gravitational lensing simulation software (*deeplens*; Morgan et al. 2021) to add LSNe to DES images in the training set. For the negative class, we use time series image sets selected at random from the data set. Even given the erroneous case where a real LSN is randomly selected for the negative training class, LSNe are expected to be sufficiently rare in the DES SN fields such that this error would be infrequent and not affect the training. Nevertheless, the two most likely types of false positives will be non-lensed SNe and strongly lensed galaxies without SNe; and unfortunately, both these types of systems are also expected to be rare in our data set. Therefore, to prepare a training set with boosted representation of systems that we expect to be more challenging to classify, we also use *deeplens* to inject lensed source galaxies and non-LSNe into a fraction of the negative-class images.

The process of injecting simulated light sources into real time series image sets has multiple benefits. The training data set includes all types of astronomical systems that the ZipperNet will classify because it is chosen from the total data set. Also, the properties of the simulated source galaxies and SNe are drawn from real data, maintaining all inherent physical correlations. We join the DES Year 3 Gold catalog and DES Year 1 morphological catalog (Tarsitano et al. 2018) to obtain a sample of $\sim 100,000$ galaxies from which we draw parameter values for simulations. The simulated source galaxies are modeled with Sérsic light profiles that have a color-independent ellipticity, a Sérsic profile index, a band-wise half-light radius, a band-wise magnitude, and a photometric redshift—all measured within DES pipelines. As in DZ1, the injected SNe were simulated using public rest-frame SN spectral energy distributions (Kessler et al. 2010) available in *deeplens*, which redshifts the distribution and calculates the observed magnitude in each band. The injected SNe reach peak brightness within the interval of 20 days before the first observation and 20 days after the final observation: the data set contains falling-only ($\sim 15\%$), rising-only ($\sim 15\%$), and complete lightcurves ($\sim 70\%$).

To calculate the lensing effects of the real galaxy on the simulated source light, we use the measured photometric redshift of the lens galaxy, select an Einstein radius at random from the interval $[0''.4, 1''.8]$, and model the mass distribution of the lens as a singular isothermal ellipsoid following similar approaches in the literature (Rojas et al. 2022). For simplicity, the mass distribution shares the measured center position and ellipticity values with the light from the real lens galaxy. This simplification is not expected to greatly affect performance because these parameters are expected to be positively correlated. From the mass profile, we calculate the lensed positions of the source galaxy and LSN, as well as account for the time delays of the separate SN images. The output of the *deeplens* simulation are time series image sets with three kinds of objects added to real DES images—LSNe, lensed source galaxies, and non-LSNe.

In total, 25% of the 76,203 time series image sets placed aside for training are injected with an LSN Ia and 25% are injected with a lensed core-collapse SN (LSN CC) to construct the positive class. Also, 16.5% of the training time series image sets are left untouched, 16.5% are injected with a galaxy–galaxy strong lens, 8.25% are injected with an SN Ia, and 8.25% are injected with an SN CC. The positive and negative training classes are equal in total number to maintain a balanced data set throughout training. We describe the details of the training in Section 3.4, but it is worth noting here that, given our choice of loss function, balancing the classes is essential to prevent class representation biasing the learned feature representation. The remainder of this subsection describes this simulation–injection process in detail. Examples of objects in the training data set are collected in Figure 1.

3.2. Preprocessing

Before we train the ZipperNet and apply it to the observed data set, we apply a series of standardization steps. We first truncate the time series image sets to 10 “time steps” in each band. A time step refers to a single exposure in the sequence of observations; in the DES SN fields, a time step is approximately 6–7 days. If an image set contains more time steps, we separate it into multiple 10-time step sequences:

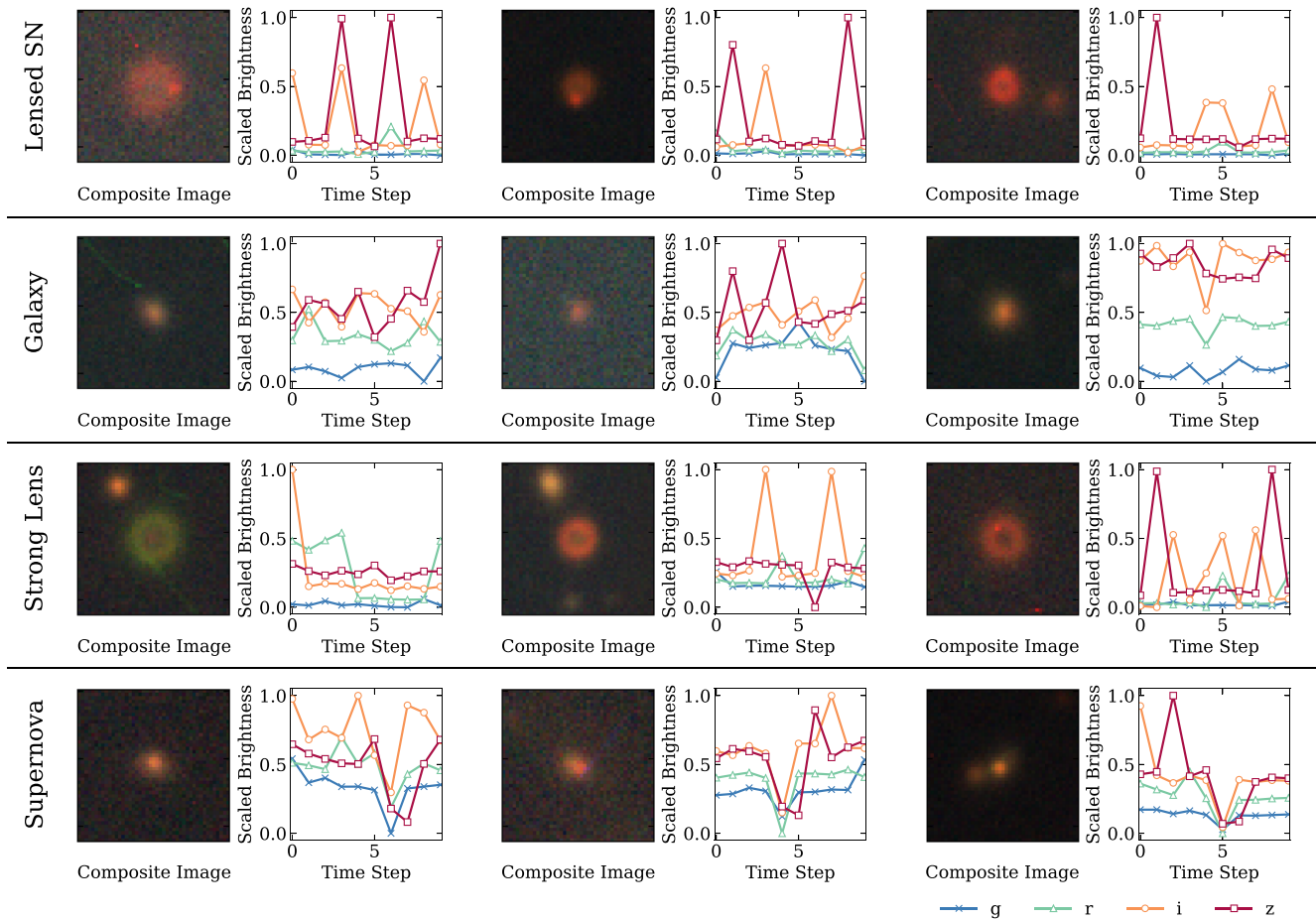


Figure 1. Examples of systems from our training data set. The composite image is an RGB visualization of the averaged *gri* images and the scaled brightnesses are the values extracted from the *g* (blue “x”), *r* (green triangles), *i* (orange circles), *z* (red squares) images at each time step in the time series image set using the aperture method presented in DZ1.

time steps 1–10 are a single sequence; time steps 2–11 are a second sequence, etc. Then, for each 10-step image sequence, we extract the total brightness as a function of time using the background-subtracted aperture technique presented in DZ1 with an aperture radius of 15 pixels. Importantly, when extracting the total brightness, the zero-point of the image is not used to maintain independence from all non-image data products. This choice produces noise-dominated extracted brightness lightcurves, such as those in Figure 1, though it is shown in the remainder of the analysis that the ZipperNet can still identify the temporal signatures of LSNs within the noise.

Next, we average the images within each band to obtain a single image in each band for the 10-step image sequence. Finally, we scale the pixel values of the averaged images and the extracted brightness values linearly to range 0 to 1 on a per-example basis. The resulting input to the ZipperNet is two different kinds of data: (1) a scaled image in each of the *gri* bands as a $4 \times 45 \times 45$ -element array and (2) a scaled 10-step lightcurve in each of the *gri* bands as a 4×10 -element array. After processing the training data set into 10-step sequences and downsampling to maintain equal representation of the positive and negative classes, we have a total of 1,000,012 training examples. We split these examples into 90% training and 10% validation data sets.

3.3. ZipperNet

The two-branch architecture of ZipperNet was first presented and validated in DZ1, and we summarize here. One branch receives scaled, time-averaged images in each band as inputs to a block that extracts convolutional features. The other branch receives scaled extracted brightness–time series as inputs to a block that extracts sequence features. The outputs from the feature-extraction blocks are flattened and concatenated. A series of fully connected layers then weights and condenses the concatenated feature representation to produce an output score that the input system contains an LSN. The ZipperNet used in this paper is similar to Figure 2 of DZ1, and the exact hyperparameter settings for this analysis are presented in Table 1.

We performed a full hyperparameter optimization of the architecture and learning algorithm using the validation data set. Small changes to hyperparameter settings from the prototype ZipperNet in DZ1 reflect a specialization for the real DES images used in the training data. We find that the addition of another convolutional layer, the addition of another long short-term memory (LSTM) layer, minor tweaks to convolutional layer kernel and stride settings, and the removal of dropout layers leads to boosted performance. The selected settings for the learning algorithm are presented in Section 3.4.

Table 1
ZipperNet Layer Specifications

Layer	Specifications
conv1 ^a	Conv2D—($k: 10, p: 2, s: 1$)—($4 \rightarrow 16$)
maxpool	MaxPool2D ($k: 2$)
conv2 ^a	Conv2D—($k: 5, p: 2, s: 1$)—($16 \rightarrow 32$)
maxpool	MaxPool2D ($k: 2$)
conv3 ^a	Conv2D—($k: 3, p: 2, s: 1$)—($32 \rightarrow 64$)
maxpool	MaxPool2D ($k: 2$)
flatten	Reshape ($12 \times 12 \times 64 \rightarrow 9216 \times 1$)
fc1 ^a	Fully connected ($9216 \rightarrow 408$)
fc2 ^a	Fully connected ($408 \rightarrow 25$)
lstm1	LSTM ($h: 128$)
lstm2	LSTM ($h: 128$)
lstm3	LSTM ($h: 128$)
fc3 ^a	Fully connected ($128 \rightarrow 50$)
concat	Concatenate fc2 and fc3 Outputs
fc4 ^a	Fully connected ($75 \rightarrow 6$)
fc5 ^b	Fully connected ($6 \rightarrow 2$)

Notes. We adopt the following shorthand: kernel size (k), padding (p), stride (s), and hidden units (h). Arrows indicate the change in the size of the data representation as it is passed through the layer.

^a Indicates a Rectified Linear Unit (ReLU) activation function.

^b Indicates a LogSoftmax activation function. In total, our model contains 4,148,225 trainable parameters.

3.4. Training

To train the ZipperNet, we implemented a distributed setup on five computers (two machines with Intel 3.2 GHz processors and 256 GB RAM, one machine with an AMD 2.2 GHz processor and 512 GB RAM, and two machines with IntelX 2.6 GHz processors and 768 GB RAM) on the DES cluster at Fermilab. The training data set was split into five equal chunks, each placed on an independent computer. On each computer, we instantiated a ZipperNet and initialized the weights at the same randomly selected values. We then begin passing the chunks of training data through the ZipperNet instances on each of the five computers. At regular intervals (every 1/15 of a chunk), we collect the parameters of each of the five ZipperNet instances and average the values of the parameters. Mathematically, the averaging operation is equivalent to the weights being updated by normal training, provided the learning rate is scaled by the number of network instances. Within this setup, we use a batch size of five examples and use stochastic gradient descent with a Nesterov momentum coefficient of 0.9, a constant learning rate of 0.001, and categorical cross-entropy loss to update the weights at each training step. We refer to the exhaustion of all data in a chunk as a “training iteration” and cycle back to the beginning of the chunk once the data has all been passed through the network instance. We allow training to continue for five training iterations and reach a final validation set accuracy of 93.0%. This raw accuracy is dependent on the representations of the different types of negative examples in the validation data set. In Section 4, we assess the performance using physically meaningful metrics.

3.5. Candidate Selection Criteria

The output of the trained ZipperNet on an input (pair of an averaged image and a lightcurve) is a score with a value

typically between -100.0 and 50.0 . Based on the minimum and maximum values of this range in our validation data set, we linearly scale the ZipperNet output scores to the range $[0.0, 1.0]$, such that they are similar to probabilities. Next, we select a threshold ZipperNet score above which we include the candidate system in our final sample and below which we exclude the candidate system. We select this threshold by iterating through possible threshold values and analyzing the fraction of LSNe that scored higher than the threshold compared to the fraction of galaxies that scored higher than the threshold. The left panel of Figure 2 shows the attainable values of these quantities for different thresholds. We expect galaxies to be the largest background: the number of galaxies in a given area of sky is orders of magnitude higher than the number of strong lenses (SLs) or SNe. Therefore, we select the threshold by reducing the fraction of galaxies scored higher than the threshold to the lowest value before the fraction of LSNe scored higher than the threshold starts to decline rapidly. Based on this analysis, we select an operating threshold for the scaled ZipperNet scores of 0.76. This threshold value is contextualized with the ZipperNet scores for the systems in our validation data set in the right panel of Figure 2.

We develop a final selection criterion to narrow the sample of candidate systems selected by ZipperNet. We leverage the aspect of our data processing from Section 3.2 in which time series image sets with more than 10 epochs are split into 10 epoch subsequences, which are then classified independently by ZipperNet. In analyzing the ZipperNet classifications made on all subsequences of a time series image set, we find that LSNe are more likely than galaxies to have multiple detections. This relationship is illustrated in Figure 3 using our validation data set, which we use as motivation to develop a criterion on the aggregate detections in a time series image set. Importantly, the total length of the time series image sets in our training and validation data was not required to match the real data as a result of our preprocessing methods, so it would be inaccurate to set a strict requirement on the number of ZipperNet detections (score above the threshold) based on the validation data set. Rather, to put the validation data set and the real data on the same footing, we set a requirement on the ratio of number of detections to number of subsequences. Therefore, we select the threshold for this ratio such that the false-positive rates (FPRs) are minimized to the point where human inspection of the final sample becomes feasible. We choose to require at least 60% of the subsequences to have a ZipperNet score above 0.76 for the candidate system to be included in our final sample of candidate LSNe. The 60% threshold and the 0.76 ZipperNet score threshold were determined simultaneously by computing the LSN recall and galaxy FPR at all possible values.

4. Results

4.1. Performance Metrics

To evaluate the performance of the fully trained ZipperNet, we define quantities and metrics of interest and compute them on the validation data set. We introduce two terms that describe classification score thresholds: “classified as an LSN” means the candidate system had a ZipperNet score greater than the threshold in at least 60% of subsequences; and “classified as background” means the candidate system had a ZipperNet score greater than the threshold in fewer than 60% of

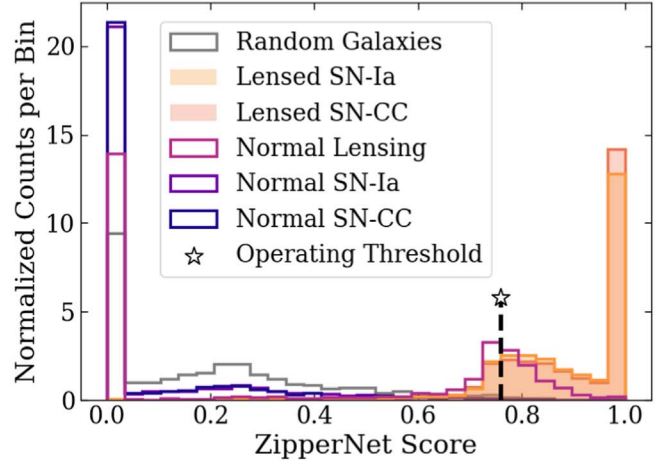
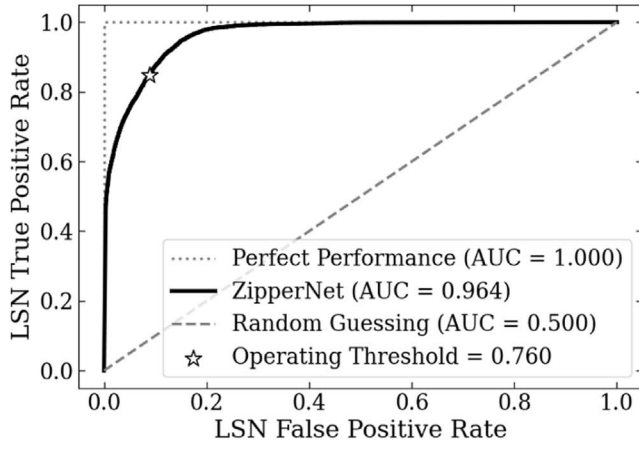


Figure 2. Left: receiver operating characteristic curve showing the lensed supernova (LSN) true-positive rate and LSN false-positive rate for all possible values of the ZipperNet operating threshold. The operating threshold of 0.760 is chosen to minimize the false positive rate to the point immediately prior to the true positive rate declining rapidly. Right: histograms of the scaled ZipperNet scores for each class in the validation data set. The selected operating threshold limits false positives from all systems in the negative class while keeping the majority of the positive class.

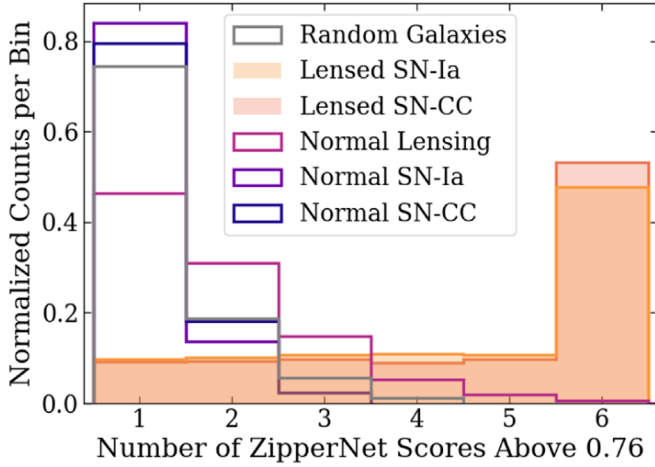


Figure 3. Number of time series image set subsequences scored above the ZipperNet threshold for each type of object in our validation data set. On average, LSNe time series image sets are scored above the ZipperNet threshold in a higher fraction of their subsequences than all types of negative examples.

subsequences. We define the following terms regarding metrics based on the threshold score:

1. a *true positive* (TP) is an LSN, and it is classified as an LSN;
2. a *false positive* (FP) is a galaxy, galaxy–galaxy lens, or unlensed SN, and it is classified as an LSN;
3. a *true negative* (TN) is a galaxy, galaxy–galaxy lens, or unlensed SN, and it is classified as background; and
4. a *false negative* (FN) is an LSN, and it is classified as background.

Using these quantities, common metrics like accuracy are straightforward to compute; however, those metrics are misleading due to the boosted representation of rare physical systems in our training and validation data sets. We instead focus on class-specific metrics that carry physical meaning and are robust against the class representation in the validation data set: the LSN recall is

$$\text{LSN Recall} = \text{TP} / (\text{TP} + \text{FN}); \quad (1)$$

Table 2

Metrics for Evaluating the Performance of ZipperNet and Our Final Sample Selection That are Robust against the Class Representations of the Validation Dataset

Metric	ZipperNet	+ Final	Equation
LSN Recall	0.8447	0.6113	Equation (1)
LSN _{Ia} Recall	0.8426	0.5949	Equation (2)
LSN _{CC} Recall	0.8468	0.6273	Equation (2)
FPR _{Galaxy}	0.0157	0.0002	Equation (3)
FPR _{SL}	0.2448	0.0046	Equation (3)
FPR _{SN-Ia}	0.0049	0.0001 ^a	Equation (3)
FPR _{SN-CC}	0.0046	0.0001 ^a	Equation (3)

Note. All metrics are defined in Section 4.1.

^a Indicates the use of an upper limit on the metric value resulting from limited statistical precision.

the LSN-type-specific recall is

$$\text{LSN}_{\text{type}} \text{ Recall} = \text{TP}_{\text{type}} / (\text{TP}_{\text{type}} + \text{FN}_{\text{type}}), \quad (2)$$

where type is “Ia” or “CC”; and the FPR for each type of negative class is

$$\text{FPR}_{\text{type}} = \text{FP}_{\text{type}} / (\text{TN}_{\text{type}} + \text{FN}_{\text{type}}), \quad (3)$$

where type is “Galaxy,” “SL,” “SN-Ia,” “SN-CC.” The values of these metrics are collected in Table 2 for ZipperNet alone and for the combination of ZipperNet with our final sample-selection criterion.

There are a few key results from these metrics worth highlighting. The ZipperNet LSN recall indicates that approximately 84% of all LSNe in the validation data set are scored above the operating threshold. The ZipperNet galaxy FPR indicates that roughly 1.5% of galaxies will be scored above our operating threshold and erroneously populate our candidate sample. By itself, the ZipperNet is a powerful classifier, but the minimized galaxy FPR is still large enough where the resulting candidate sample would be too large for visual inspection. With the addition of the selection criterion on the number of ZipperNet detections for each constituent subsequence, the performance is boosted. Critically, the final galaxy FPR is reduced, facilitating visual inspection of the full final candidate

sample. This stricter selection has the consequence of reducing the final LSN recall. However, most of the removed LSNe are those that peak before or after the window of observations.

4.2. Searching the DES SN Fields

Applying our trained ZipperNet and additional selection criterion to the DES SN field data produces 2245 candidate LSNe, approximately half of which had ZipperNet detections in multiple years of DES data. We expect the majority of these systems to have resolvable features based on two aspects of the analysis. First, these 2245 candidate LSNe were identified in the magnitude-limited sample of the DES galaxies, leading to a tendency for low-redshift, nearby galaxies to be more highly represented than high-redshift, distant galaxies. Second, based on the physical selection function of the ZipperNet on this data set (shown in Appendix A), LSNe in systems with large Einstein radii and better seeing are more likely to be recalled. Therefore, because the majority of the systems in this candidate sample should have resolvable features, human visual inspection becomes a viable approach for identifying the most interesting candidate LSNe.

A team of strong lensing experts within DES inspected six year coadded, color-composite images of the 2245 candidate LSNe systems to search for lensing, similar to how precursor strong lensing searches have been carried out. The team assigned all objects a score using the following system:

1. the detection is an image artifact, such as a diffraction spike or contamination from a bright foreground star;
2. there is a single object, such as a galaxy or star;
3. there are multiple objects with no evidence of lensing, such as SNe or clusters of galaxies;
4. there are multiple objects with evidence of lensing.

Using this system and the median score for each object, the team of inspectors identified 522, 802, 871, and 50 objects with scores “1,” “2,” “3,” and “4,” respectively. For the 50 systems with evidence of lensing, we extracted aperture lightcurves for each object in each system from the DES single-epoch images. Three systems from the 50 systems with evidence of lensing were identified to have SN-like time variability, and we upgraded their overall score to a “5.” Candidate systems scored as a “4” or “5” are presented in Figures 4 and 5, respectively, and have their properties collected in Table B1.

The 50 candidate systems scored at or above a “4” found in this analysis show evidence of lensing in their images. There are still non-lenses in this sample: for example, DES-700492744 is a high-proper-motion white dwarf appearing as a red object between two blue point sources; nevertheless, we include all systems labeled as interesting by the labeling team for completeness. Some of these systems also show evidence of point sources within the lensing configurations: there are nearly circular objects positioned within the lensing configuration. Going further, we analyze the time variability of the candidate systems by extracting five year background-subtracted lightcurves for each source in the images. The objects scored as a “5” show evidence of SN-like time variability: a short rise followed by a steady decay in brightness over the course of approximately one month as shown by Figure 5. The objects scored as a “4” do not show this temporal behavior; however, the possibility remains that some of the objects scored as a “4” are strongly lensed systems and potentially house a lensed

quasar. Section 4.3 contains a detailed presentation of the three objects scored as a “5”.

Lastly, we cross-match the 2245 ZipperNet-identified systems with the systems identified during the DES five-year photometric SN Ia cosmology analysis (Möller et al. 2022). In Möller et al., difference imaging (Kessler et al. 2015) identified 31,636 transients and SALT-II SN Ia lightcurve fitting (Guy et al. 2010) identified 2381 single-season SNe from that sample of transients. The SNe selected by lightcurve fitting are more likely to be SNe Ia than SNe CC, and most SNe CC in the total sample are also excluded by the fitting. Furthermore, this selection procedure searches for normal SNe Ia and is not adapted for possible changes in the lightcurves from the lensing. In total, there is an overlap (using a 5'' radius) of 104 systems among the ZipperNet sample and the DES SN analysis transient sample. All but four overlapping systems—DES-691702170, DES-699127397, DES-699340227, and DES-700977591—were scored as either a “2” or a “3” by the labeling team, indicating no convincing evidence for lensing. The locations of the detected transients are marked in Figure 4. Only the transient in DES-699127397 passed the SALT-II SN Ia lightcurve fitting. The difference-imaging detections in DES-699340227 and DES-700977591 appear to be spurious detections due to image subtraction errors. Lastly, while the transients detected in DES-691702170 and DES-699127397 are likely SNe, these systems do not appear to be lenses and likely should have received lower grades from the labeling team; DES-691702170 lacks an obvious lensing galaxy and the positions of the galaxies in DES-699127397 are more likely a cluster of galaxies than multiple images of the same background galaxies due to their asymmetric alignment.

Based on the SN FPRs in Table 2, this overlap is consistent with the expected ZipperNet SN background. The three systems scored as a “5” by the visual inspection team, indicating the presence of both lensing and SN-like temporal behavior, were not included in the overlapping sample. We believe the faintness of the SNe or foreground contamination for the lensing galaxy may have contributed to the non-detection from difference imaging, though a full understanding of this discrepancy is beyond the focus of our analysis.

4.3. Final LSN Candidates

The three most interesting systems identified by the ZipperNet and subsequent human visual inspection are DES-691022126, DES-701263907, and DES-699919273. We present five-year color-composite coadded images of these systems and extract lightcurves for each object of interest within them in Figure 5. From the lightcurves, the five observing seasons of the DES SN program are easily distinguishable, and we refer to each observing season as “Y1” through “Y5.” We extract the lightcurves from the single-epoch images by summing the pixels in the aperture displayed in the coadded image, subtracting the sky background measured by DES, and converting to a magnitude using the zero-point measured by DES. Importantly, the magnitudes are the combination of all objects within the aperture, so for example an SN lightcurve will contain contamination from its host galaxy. All estimated Einstein radii have been obtained by measuring the angular separations between objects, as opposed to a full modeling of the lensing system. We choose to present only the z-band lightcurves for these visualizations for simplicity, though all

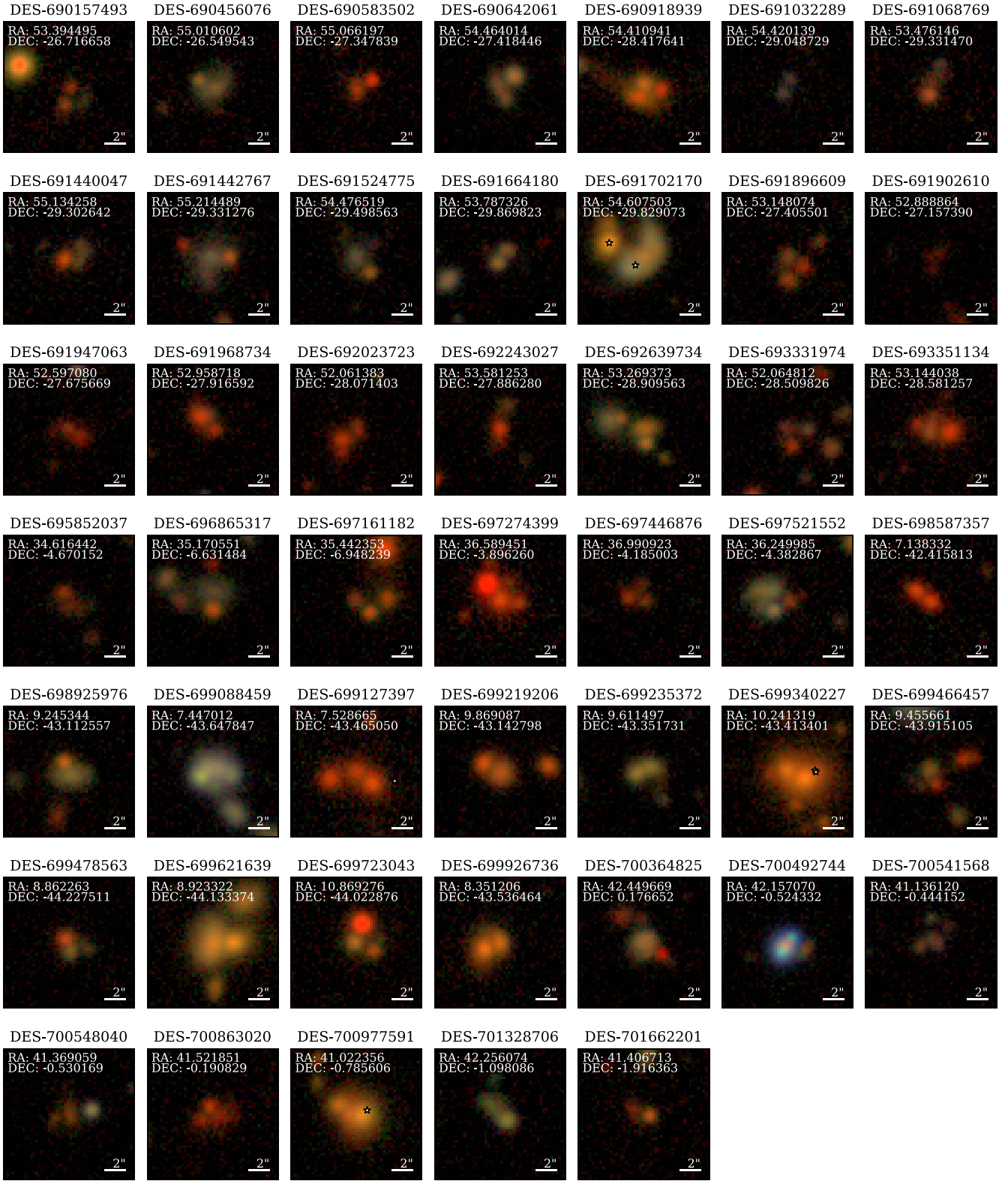


Figure 4. Candidate systems detected by ZipperNet that showed evidence of lensing but do not show SNe-like variability in their lightcurves. The properties of these candidates are collected in Table B1. Difference imaging detections from the DES SN group are shown with white star markers.

four bands were assessed to identify SN-like temporal behavior. The bluer bands such as g and r have larger PSFs in this data set compared to the redder i and z bands, leading to noisier aperture photometry measurements. Furthermore, LSNe are likely to be at high redshifts, leading to a tendency

for LSN temporal signatures to be most visible in the redder bands.

DES-691022126 is a system of four objects labeled in the top panel of Figure 5 as A, B, C, and D. We interpret objects C and D to be galaxies based on their constant brightness over

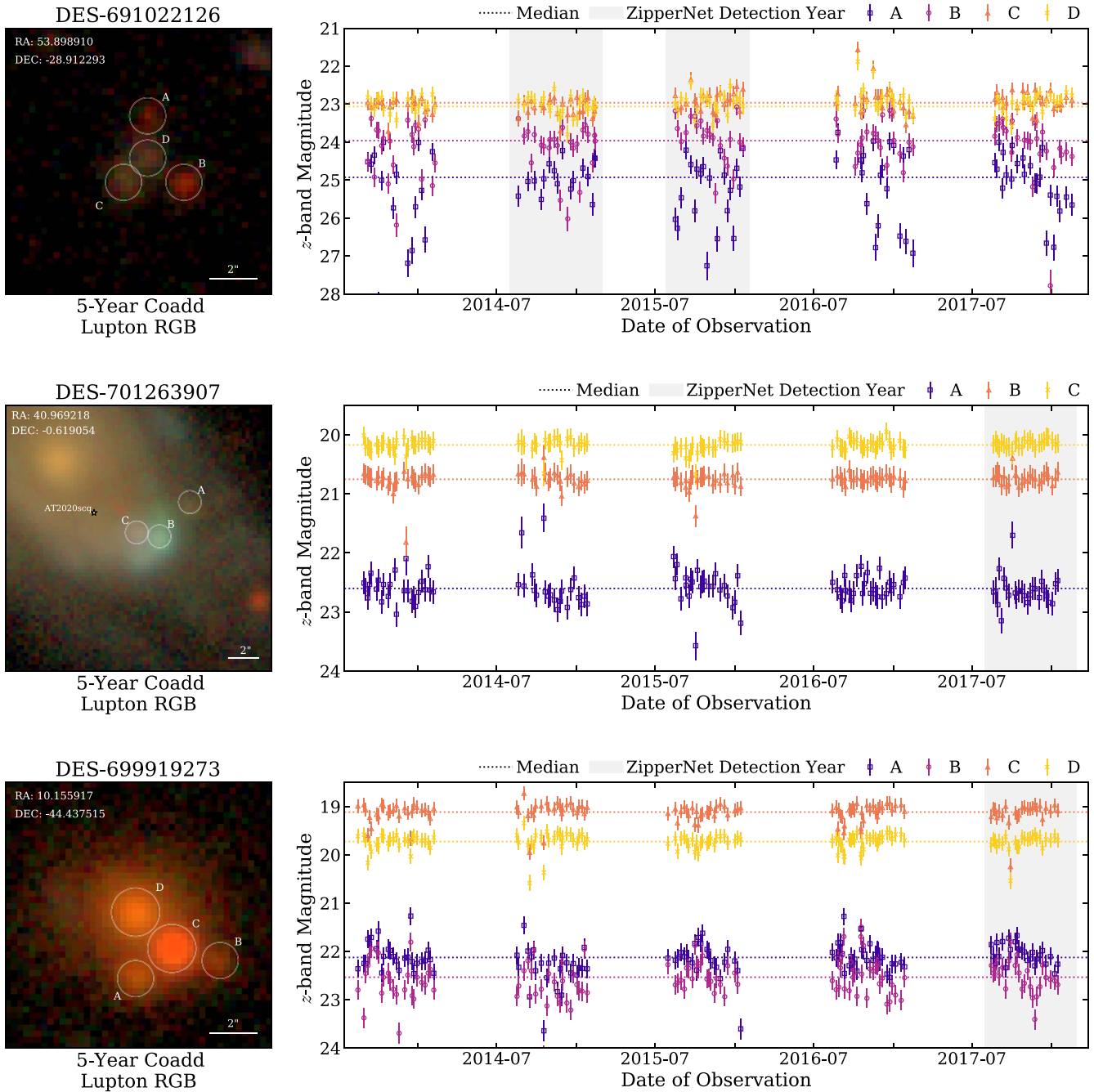


Figure 5. Candidate LSNe identified by ZipperNet and human visual inspection. The aperture used to extract the magnitude measurement from each source is shown and annotated on the coadded image. The properties of the candidates are collected in Table B1.

time. Objects A and B are much redder, and display a greater degree of brightness variability when looking at the typical size of the magnitude error bars compared to the five-year median z -band magnitude for each object. Furthermore, the lightcurves for objects A and B both contain a period of linear decline in magnitude on month timescales: object A in Y5 and object B in Y3. ZipperNet detected the system in Y2 and Y3, but not in Y5. We believe it detected the linear decline of object B in Y3 and that perhaps object C contained light from a SN between Y2 and Y3 of which ZipperNet detected the beginning. The fact that the linear decline of object A’s brightness in Y5 was not detected by ZipperNet is likely due to object A being the faintest source in the system and the selection function of ZipperNet (see the bottom right panel of Figure A). The SN-

like lightcurve features that are shared between objects A and B, when combined with the evidence for lensing with an Einstein radius of approximately $1''.7$, support the claim of the system as a LSN.

By comparison, DES-701263907 is a much more complicated system, shown in the middle panel of Figure 5. A large foreground galaxy (SIMBAD source LEDA 135660) at redshift 0.03 dominates the image. Object B (SIMBAD source SDSS J024352.54-003708.4) is cataloged as a galaxy also at redshift 0.03, but may also be a dense, star-forming region based on its blue color. This dense area, combined with the gravitational potential of LEDA 135660 itself would have a large lensing cross-section, increasing the likelihood that background objects would be lensed. Because the lightcurve extraction method

used in the lightcurves of Figure 5 does not subtract the effect of the host galaxy, the variability of these objects cannot be assessed without difference imaging techniques outside the scope of this paper. Nonetheless, we identify object A as the most variable source in the system given the foreground contamination. In the image cutout for DES-701263907, we also note the location of an SN detected in 2020 September (AT2020scq). It is possible that object B acts as a primary lensing galaxy, object A is an LSN identified by ZipperNet in 2018, and AT2020scq is a second appearance of object A delayed by approximately two years. Given the large foreground galaxies at redshift 0.03 and a potential Einstein radius of $\approx 3''$, this time delay would be consistent with an LSN.

Lastly, DES-699919273 is another four-object system that we enumerate as A, B, C, and D in the bottom panel of Figure 5. We interpret object C as the lensing galaxy, object D as an image of the source galaxy without an SN, and objects A and B as images of the source galaxy, where an SN was present at some point during DES observations. The Einstein radius for this system is $\approx 2''$. Particularly, we note a linear decline in z -band magnitude for object A in Y3 and a nearly identical linear decline in z -band magnitude for object B in Y5. ZipperNet detected the linear decline in Y5, but had no such detection in Y3. We interpret this event as another manifestation of the less-than-perfect recall of the classifier. Nonetheless, the SN-like temporal signal appearing in two of the images within a lensing geometry is evidence for the presence of an LSN.

5. Discussion

The method presented in this analysis contains a few areas where improvements could increase the LSN recall while decreasing the FPR. One such change is to add centroiding to account for sub-pixel-level shifts in position prior to stacking and averaging the images. While the offsets are small, misalignment at the $\approx 0''.25$ scale can cause image-based features to become less sharp and harder for a convolutional layer to identify. When stacking the images, it may also boost performance to only include the images with high image quality (e.g., seeing above some quality threshold and/or cloudiness below some quality threshold): this would ensure that the ability to resolve features in the resulting composite image is only limited by the instrumentation. These possibilities focus on improving the appearance of spatial features in the data to boost the ZipperNet’s ability to learn relationships and are motivated by the analysis of the physical selection function of our approach, which is described in Appendix A.

The lightcurve extraction step of the data preprocessing also could be improved by discarding common artifacts such as diffraction spikes and saturated pixels to avoid contaminating the extracted brightness. Similarly, an analysis of the clarity of features in the lightcurves as a function of the aperture radius used in the lightcurve extraction may find that a different aperture radius leads to higher performance. It is possible that scaling the time series image sets to have a standardized mean and a standardized variance of pixel value prior to preprocessing would lead to smoother lightcurves. Finally, the preprocessing steps used in this analysis down-selected images to standardize the cadence, though other approaches have demonstrated success with arbitrary numbers of images in the time series (Kodi Ramanah et al. 2022). Removing the need for a standardized cadence would greatly improve the applicability

of this approach to real-time LSN identification and remove the need for images to be discarded.

It is possible that the machine-learning aspect of the analysis could be improved with subtle changes to the training set. For example, when simulating lensed systems, we made the simplifying approximation that the mass profile ellipticity was equivalent in angle and strength to the light profile. While there is likely to be a strong correlation between the mass and light profiles, the exclusion of training set examples with different relationships between mass profile ellipticity and light profile ellipticity may bias LSN selection to systems in which these quantities are highly correlated. We also employed a uniform distribution of Einstein radii, and it is possible that an approach such as that of Kodi Ramanah et al. (2022) with a physically motivated distribution could lead to improved performance.

In consideration of a real-time LSN detection pipeline, a couple of changes to the methodology may improve performance. We envision the 10-epoch time series image sets being constructed as observations are ongoing: after a new image of a system is collected, the first image in the time series is discarded and a new 10-epoch sequence is created. There are two downsides to that approach: (1) there is an implicit requirement of 10 epochs before the trained ZipperNet can be utilized, and (2) our final selection criterion on the fraction of subsequences scored above the ZipperNet threshold requires additional epochs to create and track multiple subsequences. With the improvements to the preprocessing discussed above, it may be possible to sufficiently boost the ZipperNet performance to the point where the additional selection criterion can be removed. Furthermore, we did not experiment with time series image sets with fewer than 10 epochs, and it is possible that the analysis can be performed with a less strict requirement on the total number of epochs.

With the current configuration, we have successfully reduced a catalog of 3,459,186 objects to 2245 with our deep learning approach, and proceeded to identify 50 systems of interest through human visual inspection, three of which show some evidence of an LSN. While we do not confirm or further characterize these three systems of interest, they all contain lensing features and the presence of point sources as found during the human visual inspection. Full characterization would entail Scene Modeling Photometry (Brout et al. 2019) to obtain lightcurves without host galaxy contamination, photometric classification of that time-series photometry, redshift measurements for all objects in the system, and lens modeling, which are beyond the scope of this search. Because any detected LSNs would have faded by now, follow-up observations to confirm them are unlikely to provide any additional information apart from redshifts. However, several of the systems of interest were detected by ZipperNet in multiple years throughout DES operations. Therefore, these persistent lensed systems with point sources offer interesting candidates for lensed quasar searches. The three most interesting candidates (DES-691022126, DES-701263907, and DES-699919273) are the most likely LSNs found by our ZipperNet in the magnitude-limited five-year DES data set utilized in this analysis. Given the approximate time delays and Einstein radii of the systems, spectroscopic redshifts and lens modeling could produce three independent measurements of H_0 .

The ZipperNet architecture itself provides a new and powerful LSN identification tool going forward. The accompanying code for this analysis (DZ1) also makes the data collection, processing, simulation, training, classification, and candidate selection routines available for future analyses. With first light from the Vera C. Rubin Observatory quickly approaching, setting up a pipeline to detect LSNe is vital for time-delay cosmography measurements. The analysis presented here and suggested improvements provide a template for one such pipeline that would facilitate real-time detection of LSNe in short time series sequences of images without a dependence on traditional and computationally expensive image processing algorithms.

6. Conclusion

This analysis presents the application of a deep learning LSN detection algorithm to an observed optical survey data set. The algorithm utilizes a novel neural network architecture called a ZipperNet that simultaneously learns characteristic features from image and temporal data to identify LSNe in DES data. Using a ZipperNet trained on simulated LSNe that are injected into the DES SN field data—along with a selection criterion on the number of detections for each system—our approach performs with an LSN recall of 61.13% and an FPR of 0.02%. This technique identified 2245 candidate LSN systems in the DES SN fields, and a human visual inspection found 50 systems of interest, three of which contained evidence of a time-variable lensed source. Confirmation of these candidates of interest is left for future work, and these systems may facilitate direct measurements of H_0 when fully characterized. Looking to the Rubin Observatory era, the approach developed in DZ1 and implemented on the DES SN fields here has the potential to aid in the identification of several hundred LSNe.

R.M. thanks the Universities Research Association Fermilab Visiting Scholars Program for funding his work on this project. R.M. also thanks the LSSTC Data Science Fellowship Program, which is funded by LSSTC, NSF Cybertraining grant #1829740, the Brinson Foundation, and the Moore Foundation; his participation in the program has benefited this work.

We acknowledge the Deep Skies Lab as a community of multi-domain experts and collaborators who have facilitated an environment of open discussion, idea-generation, and collaboration. This community was important for the development of this project.

This material is based upon work supported by the National Science Foundation Graduate Research Fellowship Program under grant No. 1744555. Any opinions, findings, and conclusions or recommendations expressed in this material are those of the author(s) and do not necessarily reflect the views of the National Science Foundation.

Work supported by the Fermi National Accelerator Laboratory, managed and operated by Fermi Research Alliance, LLC under Contract No. DE-AC02-07CH11359 with the U.S. Department of Energy. The U.S. Government retains and the publisher, by accepting the article for publication, acknowledges that the U.S. Government retains a non-exclusive, paid-up, irrevocable, world-wide license to publish or reproduce the published form of this manuscript, or allow others to do so, for U.S. Government purposes.

Funding for the DES Projects has been provided by the U.S. Department of Energy, the U.S. National Science Foundation, the Ministry of Science and Education of Spain, the Science and Technology Facilities Council of the United Kingdom, the Higher Education Funding Council for England, the National Center for Supercomputing Applications at the University of Illinois at Urbana-Champaign, the Kavli Institute of Cosmological Physics at the University of Chicago, the Center for Cosmology and Astro-Particle Physics at the Ohio State University, the Mitchell Institute for Fundamental Physics and Astronomy at Texas A&M University, Financiadora de Estudos e Projetos, Fundação Carlos Chagas Filho de Amparo à Pesquisa do Estado do Rio de Janeiro, Conselho Nacional de Desenvolvimento Científico e Tecnológico and the Ministério da Ciência, Tecnologia e Inovação, the Deutsche Forschungsgemeinschaft and the Collaborating Institutions in the Dark Energy Survey.

The Collaborating Institutions are Argonne National Laboratory, the University of California at Santa Cruz, the University of Cambridge, Centro de Investigaciones Energéticas, Medioambientales y Tecnológicas-Madrid, the University of Chicago, University College London, the DES-Brazil Consortium, the University of Edinburgh, the Eidgenössische Technische Hochschule (ETH) Zürich, Fermi National Accelerator Laboratory, the University of Illinois at Urbana-Champaign, the Institut de Ciències de l'Espai (IEEC/CSIC), the Institut de Física d'Altes Energies, Lawrence Berkeley National Laboratory, the Ludwig-Maximilians Universität München and the associated Excellence Cluster Universe, the University of Michigan, NSF's NOIRLab, the University of Nottingham, The Ohio State University, the University of Pennsylvania, the University of Portsmouth, SLAC National Accelerator Laboratory, Stanford University, the University of Sussex, Texas A&M University, and the OzDES Membership Consortium.

Based in part on observations at Cerro Tololo Inter-American Observatory at NSF's NOIRLab (NOIRLab Prop. ID 2012B-0001; PI: J. Frieman), which is managed by the Association of Universities for Research in Astronomy (AURA) under a cooperative agreement with the National Science Foundation.

The DES data management system is supported by the National Science Foundation under grant Numbers AST-1138766 and AST-1536171. The DES participants from Spanish institutions are partially supported by MICINN under grants ESP2017-89838, PGC2018-094773, PGC2018-102021, SEV-2016-0588, SEV-2016-0597, and MDM-2015-0509, some of which include ERDF funds from the European Union. IFAE is partially funded by the CERCA program of the Generalitat de Catalunya. Research leading to these results has received funding from the European Research Council under the European Union's Seventh Framework Program (FP7/2007-2013) including ERC grant agreements 240672, 291329, and 306478. We acknowledge support from the Brazilian Instituto Nacional de Ciência e Tecnologia (INCT) e-Universe (CNPq grant 465376/2014-2).

This paper has gone through internal review by the DES collaboration. This manuscript has been authored by Fermi Research Alliance, LLC under Contract No. DE-AC02-07CH11359 with the U.S. Department of Energy, Office of Science, Office of High Energy Physics.

Software: `astropy` (Astropy Collaboration et al. 2013), `deeplensstronomy` (Morgan et al. 2021), `lenstronomy` (Birrer & Amara 2018; Birrer et al. 2021), `matplotlib` (Hunter 2007), `numpy` (Harris et al. 2020), `pandas` (McKinney 2010), `PlotNeuralNet` (Iqbal 2018), `PyTorch` (Paszke et al. 2019), `Scikit-Learn` (Pedregosa et al. 2011), `scipy` (Virtanen et al. 2020).

Appendix A Lensed SN Physical Selection Function

We present the selection function for our ZipperNet and our selection criterion for the number of detections. In this section, we analyze four central properties to understand the selection function of our approach: the Einstein radius, the seeing, the brightness of the source galaxy, and the brightness of the LSN. The LSN recall is calculated as a function of these four properties in Figure A1.

We find that our approach has an easier time identifying larger Einstein radii than smaller Einstein radii. Similarly, we

find that our approach has an easier time identifying LSNs in good seeing conditions than in average or poor seeing conditions. Both of these properties shed light on the importance of the clarity of spatial features in the images. Poor seeing or small Einstein radii are both situations in which image resolution is compromised and consequently spatial features become difficult or impossible to realize. This trend in algorithm performance points to data quality characteristics as opposed to a selection bias introduced by our approach. Lastly, we find that source galaxy brightness has little impact on the performance for the range applicable to this magnitude-limited analysis. We observe a similar trend for LSNs brighter than 22 mag, but notice a reduction in performance for fainter LSNs. This magnitude threshold is near the single-epoch limiting magnitude for the DES SN fields and is likely due to Malmquist bias, but there could be second-order selection effects in the detectability of the LSN images.

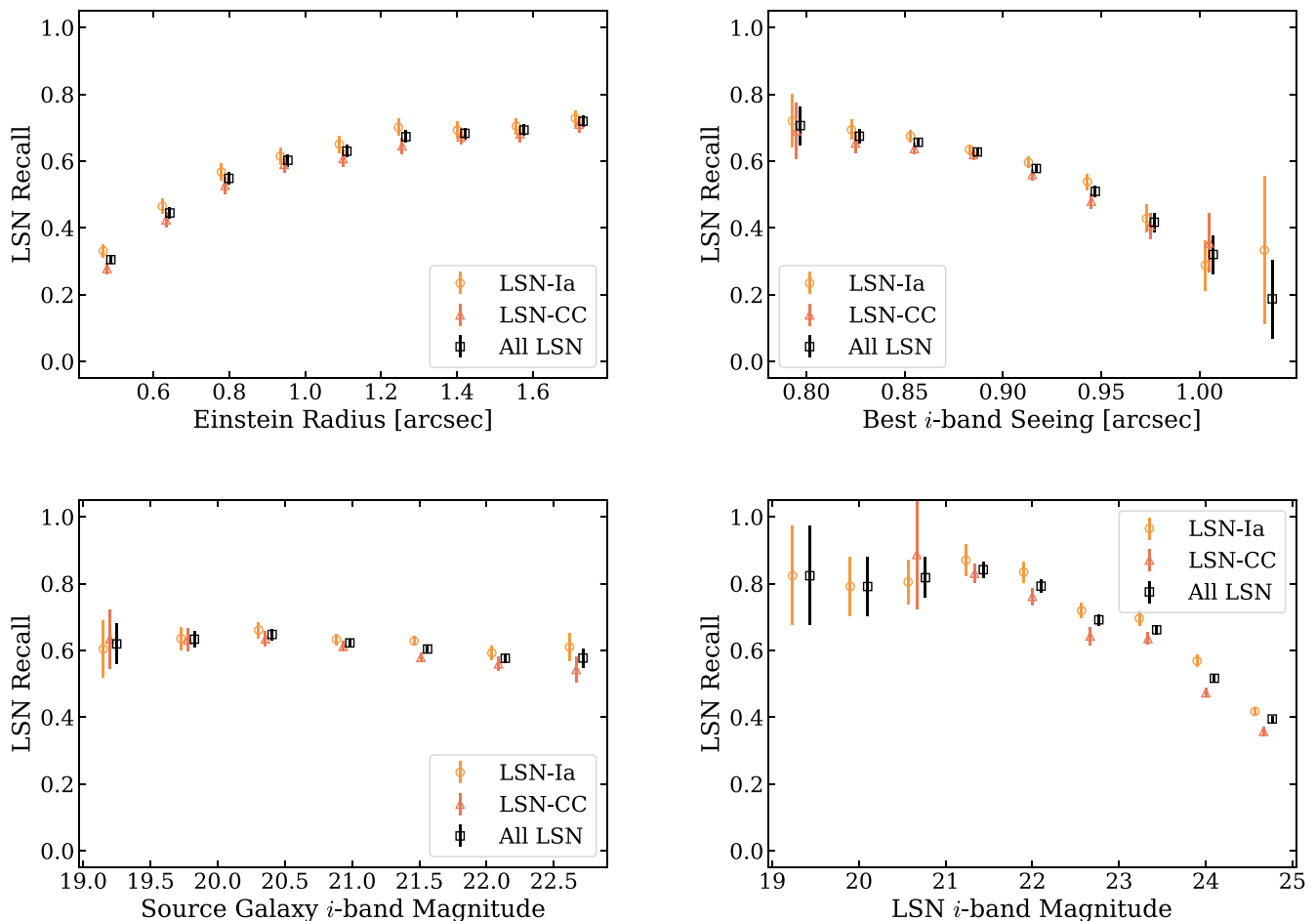


Figure A1. Physical selection function for simulated LSNs in our validation data set. We measure the LSN recall (defined in Section 4.1) as a function of Einstein radius, seeing, source galaxy unlensed magnitude, and LSN simulated unlensed magnitude. Error bars show a statistical uncertainty of one standard deviation.

Appendix B Candidate Metadata








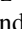











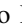









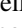



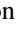











This appendix lists properties of systems detected by ZipperNet and scored as a “4” or a “5” by human visual inspection (Table B1).

Table B1
Properties of the Systems Detected by ZipperNet That Received a Score of “4” or “5” by Human Visual Inspection

No.	Coadd Id.	R.A. (deg.)	Decl. (deg.)	Mag _i	Redshift	Field	Years Detected	Inspection
1	DES-691022126	53.898910	-28.912293	21.73	...	C2	Y2 Y3	5
2	DES-701263907	40.969218	-0.619054	17.31	0.030024	S2	Y5	5
3	DES-699919273	10.155917	-44.437515	18.95	0.556	E2	Y5	5
4	DES-690157493	53.394495	-26.716658	21.82	...	C1	Y1	4
5	DES-690456076	55.010602	-26.549543	20.79	...	C1	Y1 Y2 Y3 Y4	4
6	DES-690583502	55.066197	-27.347839	21.44	...	C1	Y1 Y2 Y3 Y4 Y5	4
7	DES-690642061	54.464014	-27.418446	21.62	...	C1	Y2	4
8	DES-690918939	54.410941	-28.417641	20.65	...	C2	Y2	4
9	DES-691032289	54.420139	-29.048729	21.80	...	C2	Y2	4
10	DES-691068769	53.476146	-29.331470	20.89	...	C2	Y1 Y2 Y4 Y5	4
11	DES-691440047	55.134258	-29.302642	20.72	...	C2	Y2	4
12	DES-691442767	55.214489	-29.331276	21.79	0.139740	C2	Y4	4
13	DES-691524775	54.476519	-29.498563	21.37	...	C2	Y2	4
14	DES-691664180	53.787326	-29.869823	21.05	...	C2	Y5	4
15	DES-691702170	54.607503	-29.829073	19.42	...	C2	Y4	4
16	DES-691896609	53.148074	-27.405501	22.04	0.725	C3	Y1 Y2 Y4	4
17	DES-691902610	52.888864	-27.157390	22.37	...	C3	Y2	4
18	DES-691947063	52.597080	-27.675669	22.22	...	C3	Y1	4
19	DES-691968734	52.958718	-27.916592	21.93	0.610106	C3	Y2	4
20	DES-692023723	52.061383	-28.071403	22.20	0.949	C3	Y1 Y2 Y3 Y4 Y5	4
21	DES-692243027	53.581253	-27.886280	21.18	0.739	C3	Y4	4
22	DES-692639734	53.269373	-28.909563	21.01	0.471666	C3	Y2 Y4	4
23	DES-693331974	52.064812	-28.509826	22.47	...	C3	Y2 Y5	4
24	DES-693351134	53.144038	-28.581257	20.66	0.815070	C3	Y1 Y2 Y4 Y5	4
25	DES-695852037	34.616442	-4.670152	21.25	...	X1	Y1 Y2 Y4 Y5	4
26	DES-696865317	35.170551	-6.631484	20.56	...	X2	Y1 Y2 Y4 Y5	4
27	DES-697161182	35.442353	-6.948239	22.25	...	X2	Y1	4
28	DES-697274399	36.589451	-3.896260	20.39	0.435	X3	Y2 Y3 Y4 Y5	4
29	DES-697446876	36.990923	-4.185003	22.47	0.463	X3	Y2 Y4 Y5	4
30	DES-697521552	36.249985	-4.382867	22.23	0.798	X3	Y2 Y3 Y4 Y5	4
31	DES-698587357	7.138332	-42.415813	21.02	...	E1	Y1	4
32	DES-698925976	9.245344	-43.112557	20.18	0.318563	E1	Y2 Y4	4
33	DES-699088459	7.447012	-43.647847	18.95	...	E1	Y2	4
34	DES-699127397	7.528665	-43.465050	21.21	0.657900	E1	Y1 Y2 Y3 Y4 Y5	4
35	DES-699219206	9.869087	-43.142798	20.47	...	E2	Y2	4
36	DES-699235372	9.611497	-43.351731	20.46	...	E2	Y2	4
37	DES-699340227	10.241319	-43.413401	20.32	...	E2	Y1 Y2 Y3 Y4 Y5	4
38	DES-699466457	9.455661	-43.915105	22.19	0.469	E2	Y1	4
39	DES-699478563	8.862263	-44.227511	20.67	0.751	E2	Y2	4
40	DES-699621639	8.923322	-44.133374	19.12	0.235	E2	Y1 Y2	4
41	DES-699723043	10.869276	-44.022876	21.71	...	E2	Y1 Y2 Y3 Y5	4
42	DES-699926736	8.351206	-43.536464	21.14	...	E1	Y1 Y2 Y4 Y5	4
43	DES-700364825	42.449669	0.176652	20.46	...	S1	Y4	4
44	DES-700492744	42.157070	-0.524332	19.30	...	S1	Y5	4
45	DES-700541568	41.136120	-0.444152	21.63	...	S2	Y4	4
46	DES-700548040	41.369059	-0.530169	21.29	...	S2	Y1 Y2 Y4	4
47	DES-700863020	41.521851	-0.190829	20.52	...	S2	Y2	4
48	DES-700977591	41.022356	-0.785606	18.75	0.287564	S2	Y1 Y2 Y5	4
49	DES-701328706	42.256074	-1.098086	20.76	...	S2	Y1	4
50	DES-701662201	41.406713	-1.916363	21.23	...	S2	Y3	4

Note. The “Coadd Id.” is from the DES Y3 GOLD Catalog. The “Years Detected” indicate the years of DES data collection during which the candidate was selected by ZipperNet. The “Redshift” values are either photometric estimates from DES (shown to three significant digits) or spectroscopic measurements from OzDES (Yuan et al. 2015) and refer to the candidate lensing galaxy.

ORCID iDs

R. Morgan  <https://orcid.org/0000-0002-7016-5471>
 B. Nord  <https://orcid.org/0000-0001-6706-8972>
 K. Bechtol  <https://orcid.org/0000-0001-8156-0429>
 A. Möller  <https://orcid.org/0000-0001-8211-8608>
 S. Birrer  <https://orcid.org/0000-0003-3195-5507>
 S. J. González  <https://orcid.org/0000-0001-7282-3864>
 M. Martinez  <https://orcid.org/0000-0002-8397-8412>
 R. A. Gruendl  <https://orcid.org/0000-0002-4588-6517>
 E. J. Buckley-Geer  <https://orcid.org/0000-0002-3304-0733>
 A. J. Shajib  <https://orcid.org/0000-0002-5558-888X>
 A. Carnero Rosell  <https://orcid.org/0000-0003-3044-5150>
 C. Lidman  <https://orcid.org/0000-0003-1731-0497>
 T. Collett  <https://orcid.org/0000-0001-5564-3140>
 M. Aguena  <https://orcid.org/0000-0001-5679-6747>
 J. Annis  <https://orcid.org/0000-0002-0609-3987>
 D. Bacon  <https://orcid.org/0000-0002-2562-8537>
 S. Bocquet  <https://orcid.org/0000-0002-4900-805X>
 D. Brooks  <https://orcid.org/0000-0002-8458-5047>
 M. Carrasco Kind  <https://orcid.org/0000-0002-4802-3194>
 J. Carretero  <https://orcid.org/0000-0002-3130-0204>
 F. J. Castander  <https://orcid.org/0000-0001-7316-4573>
 C. Conselice  <https://orcid.org/0000-0003-1949-7638>
 M. Costanzi  <https://orcid.org/0000-0001-8158-1449>
 J. De Vicente  <https://orcid.org/0000-0001-8318-6813>
 S. Desai  <https://orcid.org/0000-0002-0466-3288>
 B. Flaugher  <https://orcid.org/0000-0002-2367-5049>
 J. Frieman  <https://orcid.org/0000-0003-4079-3263>
 J. García-Bellido  <https://orcid.org/0000-0002-9370-8360>
 E. Gaztanaga  <https://orcid.org/0000-0001-9632-0815>
 D. Gruen  <https://orcid.org/0000-0003-3270-7644>
 G. Gutierrez  <https://orcid.org/0000-0003-0825-0517>
 S. R. Hinton  <https://orcid.org/0000-0003-2071-9349>
 D. L. Hollowood  <https://orcid.org/0000-0002-9369-4157>
 K. Honscheid  <https://orcid.org/0000-0002-6550-2023>
 K. Kuehn  <https://orcid.org/0000-0003-0120-0808>
 N. Kuropatkin  <https://orcid.org/0000-0003-2511-0946>
 O. Lahav  <https://orcid.org/0000-0002-1134-9035>
 F. Menanteau  <https://orcid.org/0000-0002-1372-2534>
 R. Miquel  <https://orcid.org/0000-0002-6610-4836>
 A. Palmese  <https://orcid.org/0000-0002-6011-0530>
 F. Paz-Chinchón  <https://orcid.org/0000-0003-1339-2683>
 A. Pieres  <https://orcid.org/0000-0001-9186-6042>
 A. A. Plazas Malagón  <https://orcid.org/0000-0002-2598-0514>
 A. K. Romer  <https://orcid.org/0000-0002-9328-879X>
 A. Roodman  <https://orcid.org/0000-0001-5326-3486>

E. Sanchez  <https://orcid.org/0000-0002-9646-8198>
 I. Sevilla-Noarbe  <https://orcid.org/0000-0002-1831-1953>
 M. Smith  <https://orcid.org/0000-0002-3321-1432>
 E. Suchyta  <https://orcid.org/0000-0002-7047-9358>
 G. Tarle  <https://orcid.org/0000-0003-1704-0781>

References

- Abbott, T., Abdalla, F. B., Aleksić, J., et al. 2016, *MNRAS*, 460, 1270
 Abbott, T. M. C., Abdalla, F. B., Allam, S., et al. 2018, *ApJS*, 239, 18
 Abbott, T. M. C., Adamów, M., Aguena, M., et al. 2021, *ApJS*, 255, 20
 Amanullah, R., Goobar, A., Clément, B., et al. 2011, *ApJL*, 742, L7
 Astropy Collaboration, Robitaille, T. P., Tollerud, E. J., et al. 2013, *A&A*, 558, A33
 Birrer, S., & Amara, A. 2018, *PDU*, 22, 189
 Birrer, S., Shajib, A. J., Gilman, D., et al. 2021, *JOSS*, 6, 3283
 Brout, D., Sako, M., Scolnic, D., et al. 2019, *ApJ*, 874, 106
 Diehl, H. T. 2020, The Dark Energy Survey and Operations: Year 6 – The Finale. <https://www.osti.gov/biblio/1596042/>
 Flaugher, B., Diehl, H. T., Honscheid, K., et al. 2015, *AJ*, 150, 150
 Goobar, A., Amanullah, R., Kulkarni, S. R., et al. 2017, *Sci*, 356, 291
 Graham, M. J., Kulkarni, S. R., Bellm, E. C., et al. 2019, *PASP*, 131, 078001
 Guy, J., Sullivan, M., Conley, A., et al. 2010, *A&A*, 523, A7
 Harris, C. R., Millman, K. J., van der Walt, S. J., et al. 2020, *Natur*, 585, 357
 Hartley, W. G., Choi, A., Amon, A., et al. 2021, *MNRAS*, 509, 3547
 Hunter, J. D. 2007, *CSE*, 9, 90
 Iqbal, H. 2018, PlotNeuralNet v1.0.0, Zenodo, doi:10.5281/zenodo.2526396
 Jones, D. O., Foley, R. J., Narayan, G., et al. 2021, *ApJ*, 908, 143
 Ivezić, Ž., Kahn, S. M., Tyson, J. A., et al. 2019, *ApJ*, 873, 111
 Kelly, P. L., Rodney, S. A., Treu, T., et al. 2015, *Sci*, 347, 1123
 Kessler, R., Bassett, B., Belov, P., et al. 2010, *PASP*, 122, 1415
 Kessler, R., Marriner, J., Childress, M., et al. 2015, *AJ*, 150, 172
 Kodi Ramanah, D., Arendse, N., & Wojtak, R. 2022, *MNRAS*, 512, 5404
 Marshall, P., Anguita, T., Bianco, F. B., et al. 2017, arXiv:1708.04058
 McKinney, W. 2010, in Proc. of the 9th Python in Science Conf., 445, ed. Stéfan van der Walt & Jarrod Millman (Austin, TX: SciPy), 56
 Mihalas, D. 1963, *PASP*, 75, 256
 Möller, A., Smith, M., Sako, M., et al. 2022, *MNRAS*, 514, 5159
 Morgan, R. 2022, DeepZipper II: Analysis and Data Processing Code, Zenodo, doi:10.5281/zenodo.6419722
 Morgan, R., Nord, B., Bechtol, K., et al. 2022, *ApJ*, 927, 109
 Morgan, R., Nord, B., Birrer, S., Lin, J. Y.-Y., & Poh, J. 2021, *JOSS*, 6, 2854
 Oguri, M. 2019, *RPPH*, 82, 126901
 Paszke, A., Gross, S., Massa, F., et al. 2019, arXiv:1912.01703
 Pedregosa, F., Varoquaux, G., Gramfort, A., et al. 2011, *JMLR*, 12, 2825
 Quimby, R. M., Oguri, M., More, A., et al. 2014, *Sci*, 344, 396
 Refsdal, S. 1964, *MNRAS*, 128, 307
 Rodney, S. A., Brammer, G. B., Pierel, J. D. R., et al. 2021, *NatAs*, 5, 1118
 Rodney, S. A., Patel, B., Scolnic, D., et al. 2015, *ApJ*, 811, 70
 Rojas, K., Savary, E., Clément, B., et al. 2022, *A&A*, 668, A73
 Tarsitano, F., Hartley, W. G., Amara, A., et al. 2018, *MNRAS*, 481, 2018
 Treu, T. 2010, *ARA&A*, 48, 87
 Virtanen, P., Gommers, R., Oliphant, T. E., et al. 2020, *NatMe*, 17, 261
 Yuan, F., Lidman, C., Davis, T. M., et al. 2015, *MNRAS*, 452, 3047